JSWSC

Available online at:
www.swsc-journal.org

Topical Issue - Severe space weather events of May 2024 and their impacts

RESEARCH ARTICLE

OPEN 2 ACCESS

Real-time precise point positioning performance in Hong Kong during May 2024 space weather events

Mengfei Sun¹, Tong Liu², Jian Liu¹, Kun Zhang¹, Junting Huang¹, and Bo Chen^{1,*}

Received 26 December 2024 / Accepted 10 July 2025

Abstract-Space weather events are the primary drivers of ionospheric variations. These variations challenge conventional GNSS algorithms' ionospheric processing strategies, leading to degraded positioning accuracy. In low-latitude regions during extreme events, the coupling of space weather effects with inherent low-latitude ionospheric anomalies makes it challenging to understand the mechanisms behind the decline in Global Navigation Satellite System (GNSS) positioning accuracy, continuity, and availability. This poses a significant challenge for users relying on real-time Precise Point Positioning (PPP). To investigate the impact of the May 2024 space weather events on real-time PPP, we evaluated and analyzed the ionospheric responses, as well as the positioning performance of dual-frequency Ionosphere-Free PPP (IF-PPP) and Undifferenced Uncombined PPP (UDUC-PPP), using Quasi-Zenith Satellite System (QZSS) L6 band (1278.75 MHz) data in Hong Kong. The results demonstrate that, during this event, daily positioning accuracy degraded from centimeter to decimeter levels, and in severe instances, positioning results became unavailable. The degradation in positioning accuracy for both IF-PPP and UDUC-PPP showed a clear correlation with ionospheric conditions, particularly during scintillation, which led to the failure of cycle slip detection algorithms and deterioration of observation quality. L1 band (1575.42 MHz) pseudorange measurements showed better resistance to ionospheric scintillation than L2 band (1227.60 MHz). Additionally, we identified different mechanisms by which the ionosphere affects the IF-PPP and UDUC models during these periods, and the possible ionospheric phenomena associated with positioning accuracy in low latitudes.

Keywords: Space weather events / Ionospheric scintillation / UDUC-PPP / Real-time GNSS positioning / QZSS L6

1 Introduction

Coronal mass ejections (CMEs) and solar flares – primary space weather events – may generate geomagnetic disturbances linked to ionospheric irregularities (Matamba et al., 2023). Although geomagnetic storms could modulate irregularity characteristics, they do not directly initiate them (González, 2022). At low latitudes, including Hong Kong, these irregularities frequently intensify through mechanisms like the Equatorial Ionization Anomaly (EIA) and Plasma Bubbles (EPBs) (Smith & Heelis, 2017; Aa et al., 2020; Sergeeva, 2022), while statistical patterns show that the occurrence of irregularities correlates with active solar phases (Liu et al., 2022). Although significant irregularities may originate independently from tropospheric gravity waves or lightning (Liu et al., 2021; Nie et al., 2024), space weather remains the predominant underlying driver. The May 2024 geomagnetic storm (Dst-index: –412 nT

on DOY 132, ranked sixth largest since 1957) may exemplify such modulation scenarios (Förster & Jakowski, 2000), potentially degrading real-time GNSS performance.

The impact of space weather on positioning is closely related to the processing method (Warnant et al., 2007). Based on the varying user requirements for positioning timeliness, positioning methods can be categorized into post-processed and real-time methods (Xu & Xu, 2016). For geodesy users, like deformation monitoring, post-processing methods are often used. Post-processing methods include differential positioning and post-processed Precise Point Positioning (PPP), which involves obtaining an absolute position using a single receiver with precise orbit products (Kouba & Héroux, 2001). The influence of each space weather event varies, requiring individual analysis (Demyanov & Yasyukevich, 2021; Chen et al., 2023; Afraimovich et al., 2008). For the Solar Radio Burst Events on September 6, 2017, Sato et al. (2019) evaluated PPP performance at European GNSS stations, showing intense space weather degrades performance across frequencies.

¹ School of Aerospace, Harbin Institute of Technology Shenzhen, Shenzhen, PR China

² The Hong Kong Polytechnic University, Hong Kong, PR China

^{*}Corresponding author: hitchenbo@hit.edu.cn

Yasyukevich et al. (2018) found that GPS PPP errors during solar flare events exceeded background levels by three times. During the 2015 St. Patrick's Day storm Jacobsen & Andalsvik (2016) observed that positioning errors in Norway increased rapidly with the Rate of TEC Index (ROTI). Lu et al. (2020) analyzed PPP performance in Hong Kong during the storm, noting that frequent cycle slips led to re-convergence and reduced accuracy. In ionospheric perturbation events, Luo et al. (2018) studied the kinematic PPP performance of the BeiDou Navigation Satellite System (BDS) under ionospheric scintillation in low-latitude regions, finding significant errors in the East (E). North (N), and Up (U) directions. Zakharenkova & Cherniak (2021) examined GPS kinematic PPP under EPBs conditions in the United States. Zhang et al. (2014) proposed a robust approach to enhance accuracy during ionospheric scintillation by relaxing the cycle slip detection threshold. Nie et al. (2022) improved single-frequency kinematic PPP positioning under solar flare conditions. Aquino et al. (2009) mitigated GNSS errors during ionospheric scintillation by refining the stochastic model. In summary, while space weather events impact PPP, various strategies, such as post-processed regional error correction products and the backward filtering method, can help mitigate these effects. However, for users relying on autonomous driving, smartphone navigation, drones, and commercial aviation, there is a strong demand for real-time solutions, making post-processing strategies ineffective. This underscores the importance of studying space weather's impact on real-time PPP (De Bakker & Tiberius, 2017; Zuo et al., 2022).

Real-time positioning techniques are categorized into relative and absolute positioning. Relative positioning requires differential corrections from a reference station, with Real-Time Kinematic (RTK) being the most widely used (Alkan et al., 2020). Studies have shown that RTK accuracy degrades during ionospheric disturbances (Lejeune & Warnant, 2008; Paziewski & Sieradzki, 2020; Follestad et al., 2021). RTK requires corrections from reference stations, and although it is also affected by space weather, the ionospheric corrections provided by these reference stations can alleviate the impact (Leick et al., 2015). In contrast, absolute positioning, i.e., PPP, only needs one receiver with external data, making it more susceptible to space weather events. The commonly used method for absolute positioning is real-time PPP (Elsobeiey & Al-Harbi, 2016; Pan et al., 2017). Real-time PPP relies on external precise products mainly provided by the IGS Real-Time Service (RTS) and satellite services (Muellerschoen et al., 2001). Satellite PPP services, such as the QZSS L6 signal, BDS PPP-B2b signal, and Galileo HAS service are crucial for the next generation due to their unrestricted availability, unlike the IGS RTS, which requires ground network communication (Namie & Kubo, 2021; Fernandez-Hernandez et al., 2022; Yang et al., 2022). Real-time PPP models are categorized based on how they handle ionospheric delay: Ionosphere-Free PPP (IF-PPP) and Undifferenced and Uncombined PPP (UDUC-PPP). IF-PPP eliminates the first-order ionospheric term by combining dual-frequency pseudorange and phase observations (Zumberge et al., 1997; Kouba & Héroux, 2001). UDUC-PPP estimates ionospheric delays directly, avoiding noise amplification from combination methods (Guo et al., 2016a). However, there is a lack of comprehensive studies on the impact of space weather events on real-time satellite PPP performance, including IF-PPP and UDUC-PPP (Jacobsen, 2014; Muhammad et al., 2015; Liu et al., 2018). Therefore, studying the effects of space weather events on real-time PPP at low-latitudes can enhance our ability to respond to space environment changes and improve GNSS's robustness. In particular, the intense solar eruptions in May 2024, which resulted in an extreme geomagnetic storm and auroral expansion, warrant detailed investigation (Bojilova et al., 2024; Lazzús & Salfate, 2024).

In light of these challenges, we analyzed the performance of real-time PPP using QZSS L6 corrections under the space weather conditions of May 2024. The remainder of this paper is organized as follows: Section 2 describes the data used in this study. Section 3 details the space weather conditions and ionospheric responses during May 2024. Section 4 outlines the positioning model and ionospheric processing methods. Section 5 presents the results and analysis. Section 6 concludes the paper.

2 Dataset

In this section, we introduce the dataset used for calculating parameters describing the ionosphere in Section 2.1 and the dataset required for the real-time PPP based on QZSS L6 signals in Section 2.2.

2.1 Dataset used for calculating ionospheric parameters

We utilize GPS data from 18 stations of the Hong Kong Satellite Positioning Reference Station Network, along with the corresponding broadcast ephemerides and satellite Differential Code Bias (DCB) files from the Center for Orbit Determination in Europe (CODE) (Montenbruck et al., 2014). All GPS observation files are standardized to the RINEX 2.11 format. The data spanned from May 1, 2024 to May 15, 2024 (Day of Year 122 to Day of Year 136) and were sampled at a rate of 1 s. Table 1 provides detailed information about the stations used, and Figure 1 illustrates their geographical locations.

2.2 Dataset used for real-time PPP

The data used for real-time PPP with QZSS L6 include RINEX observation data, broadcast ephemeris data, ATX antenna data, and QZSS L6 correction data.

RINEX and ATX Files. The RINEX observation files are obtained from 18 GPS stations in Hong Kong, which are the same stations used for calculating ionospheric parameters and standardized to the RINEX 2.11 format. Detailed descriptions and geographic distributions are provided in Table 1 and Figure 1. The only difference is that the observation sampling rate is 30 s. ATX files contain antenna phase center offset (PCO) and phase center variation (PCV) calibration information, which is primarily used to improve the accuracy of calculations in satellite navigation systems (Rothacher & Schmid, 2010).

QZSS L6 Correction Data and Preprocessing. The Quasi-Zenith Satellite System (QZSS) Multi-GNSS Advanced Orbit and Clock Augmentation – Precise Point Positioning (MADOCA-PPP) service began offering trial services to users in the Asia-Pacific region (from 60°S to 60°N and 70°E to 200°E) in 2022 (Kawate et al., 2023). The L6E messages are

Table 1. Details of the 18 GPS stations used for ionospheric response and PPP.

RINEX ID	Latitude [°]	Longtitude [°]	Height [m]
HKKT	22.4449	114.0665	34.5764
HKLM	22.2189	114.1200	8.5536
HKLT	22.4181	113.9966	125.9221
HKMW	22.2558	114.0031	194.9461
HKNP	22.2490	113.8938	350.6723
HKOH	22.2476	114.2285	166.4011
HKPC	22.2849	114.0378	18.1303
HKQT	22.2910	114.2132	47.57760
HKSC	22.3221	114.1411	20.2386
HKSL	22.3720	113.9279	95.2972
HKSS	22.4310	114.2692	38.7135
HKST	22.3952	114.1842	258.7045
HKTK	22.5465	114.2232	22.5335
HKWS	22.4342	114.3353	63.7909
KYC1	22.2840	114.0763	116.319
HKCL	22.2958	113.9077	7.647
HKFN	22.4946	114.1381	41.157
T430	22.4947	114.1382	41.261

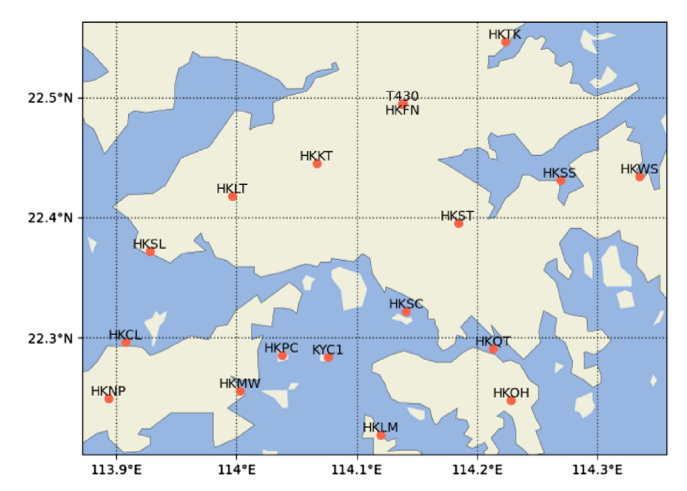


Figure 1. The geographical locations of 18 GPS stations.

binary files in Compact SSR format, containing clock and ephemeris corrections. Combined with broadcast ephemerides, these provide satellite clock and orbit corrections. The specific algorithm for correcting satellite clock bias is as follows:

$$t_{\rm sat} = t_{\rm broa} - \frac{\delta C}{c},\tag{1}$$

where $t_{\rm sat}$ represents the corrected satellite clock bias, "broa" denotes the satellite clock bias from the broadcast ephemeris, δC is the L6 clock correction, and c is the speed of light.

The algorithm for correcting satellite orbits is as follows:

$$\mathbf{X}_{\text{orbit}} = \mathbf{r} - \delta \mathbf{X},\tag{2}$$

where $\mathbf{X}_{\text{orbit}}$ represents the corrected satellite orbit, \mathbf{r} denotes the satellite position from the broadcast ephemeris, and $\delta \mathbf{X}$ is the correction term calculated based on the L6 signal. It is computed using the following equation:

$$\delta \mathbf{X} = \begin{bmatrix} e_{\text{radial}} & e_{\text{along}} & e_{\text{cross}} \end{bmatrix} \begin{bmatrix} \delta O_{\text{radial}} \\ \delta O_{\text{along}} \\ \delta O_{\text{cross}} \end{bmatrix}, \tag{3}$$

where:

$$e_{\text{along}} = \frac{\dot{\mathbf{r}}(t)}{|\dot{\mathbf{r}}(t)|},\tag{4}$$

$$e_{\text{cross}} = \frac{\mathbf{r}(t) \times \dot{\mathbf{r}}(t)}{|\mathbf{r}(t) \times \dot{\mathbf{r}}(t)|},$$
 (5)

$$e_{\text{radial}} = \mathbf{e}_{\text{along}}(t) \times \mathbf{e}_{\text{cross}}(t),$$
 (6)

where $e_{\rm radial}, e_{\rm along}$, and $e_{\rm cross}$ represent the unit vectors in the radial, along-track, and cross-track directions, respectively. $\delta O_{\rm radial}, \ \delta O_{\rm along}, \ {\rm and} \ \delta O_{\rm cross}$ represent the compact SSR corrections for the radial, along-track, and cross-track components, respectively. $\dot{\bf r}$ denotes the satellite speed calculated from the broadcast ephemeris, and t represents time.

3 Space weather conditions and ionospheric responses

In this section, we first describe the space weather conditions during the first half of May 2024 in Section 3.1. Then, Section 3.2 details the ionospheric response to these space weather events above Hong Kong.

3.1 Space weather conditions of May 2024

In May 2024, as solar activity intensified, various space weather events occurred. These included solar flares, associated coronal mass ejections (CMEs), and extreme geomagnetic storms, notably triggered on May 10, 2024.

A solar flare is a sudden and intense burst of energy on the Sun, marked by the emission of electromagnetic radiation across the spectrum and a rapid increase in brightness in a localized area on the Sun's surface (Gosling, 1993). These events are categorized based on their intensity and effects on Earth. Solar flares are classified into five categories – A, B, C, M, and X – based on their X-ray brightness in the 1 to 8 Angstrom wavelength range, with X being the most intense. Intense solar flares, primarily X-class and occasionally M-class, release X-rays and extreme ultraviolet (EUV) radiation that reach Earth in about 8 min, causing a rapid increase in ionospheric electron density. This leads to significant ionospheric disturbances on the sunlit side of Earth (Tsurutani et al., 2009). Between May 1 and May 15, 21 X-class solar flares were detected by the X-ray and Extreme UV sensors aboard GOES satellites (Schuh et al., 2016; Machol et al., 2020). Table 2 summarizes the solar flare events that affected the sunlit side of the Earth.

Solar flares are often accompanied by CMEs, which involve the significant release of plasma and magnetic fields from the Sun's corona. These ejected materials can disrupt the solar wind. When the plasma and magnetic fields reach Earth's space environment, they can interact with the geomagnetic field, potentially destabilizing the magnetosphere (Schwenn, 2006). Unlike the electromagnetic radiation from solar flares, CMEs

Table 2. Solar flare events during the first half of May 2024.

Event ID	Start	Stop	Peak	GOES Class
1	2024-05-03 02:11 UTC	2024-05-03 02:27:00 UTC	2024-05-03 02:22:00 UTC	X1.7
	DOY 124 10:11 LT	DOY 124 10:27:00 LT	DOY 124 10:22:00 LT	
2	2024-05-05 05:47 UTC	2024-05-05 06:07:00 UTC	2024-05-05 06:01:00 UTC	X1.3
	DOY 126 13:47 LT	DOY 126 14:07:00 LT	DOY 126 14:01:00 LT	
3	2024-05-06 05:38 UTC	2024-05-06 06:52:25 UTC	2024-05-06 06:35:00 UTC	X4.5
	DOY 127 13:38 LT	DOY 127 14:52:25 LT	DOY 127 14:35:00 LT	
4	2024-05-08 01:33 UTC	2024-05-08 01:48:00 UTC	2024-05-08 01:41:00 UTC	X1.0
	DOY 129 09:33 LT	DOY 129 09:48:00 LT	DOY 129 09:41:00 LT	
5	2024-05-08 04:37 UTC	2024-05-08 05:28:20 UTC	2024-05-08 05:09:00 UTC	X1.0
	DOY 129 12:37 LT	DOY 129 13:28:20 LT	DOY 129 13:09:00 LT	
6	2024-05-09 08:45 UTC	2024-05-09 09:31:20 UTC	2024-05-09 09:13:00 UTC	X2.3
	DOY 130 16:45 LT	DOY 130 17:31:20 LT	DOY 130 17:13:00 LT	
7	2024-05-10 06:27 UTC	2024-05-10 07:13:19 UTC	2024-05-10 06:54:00 UTC	X4.0
	DOY 131 14:27 LT	DOY 131 15:13:19 LT	DOY 131 14:54:00 LT	
8	2024-05-11 01:10 UTC	2024-05-11 01:39:00 UTC	2024-05-11 01:23:00 UTC	X5.8
	DOY 132 09:10 LT	DOY 132 09:39:00 LT	DOY 132 09:23:00 LT	
9	2024-05-14 02:03 UTC	2024-05-14 02:19:00 UTC	2024-05-14 02:09:00 UTC	X1.7
	DOY 135 10:03 LT	DOY 135 10:19:00 LT	DOY 135 10:09:00 LT	
10	2024-05-15 08:18 UTC	2024-05-15 08:55:34 UTC	2024-05-15 08:37:00 UTC	X3.5
	DOY 136 16:18 LT	DOY 136 16:55:34 LT	DOY 136 16:37:00 LT	

typically take 1–3 days to reach Earth (Balasis et al., 2019). From May 5 to May 15, 2024, the Large Angle Spectrometric Coronagraph (LASCO) observed at least 20 major CMEs with widths greater than 60° (Brueckner et al., 1995). Specific CME events are listed in Table 3 (Hayakawa et al., 2024).

Figure 2 illustrates the Interplanetary Magnetic Field (IMF) and the Sym-H index during this geomagnetic storm. The IMF magnitude and its Bz component provide insights into the processes occurring in the interplanetary medium and solar wind, characterizing the interaction between the solar wind and Earth's magnetosphere. The Sym-H index, similar to the Dstindex but with a 1-minute resolution, is based on data from six longitudinally distributed stations (Iyemori et al., 2010) and reflects global magnetic disturbances in the equatorial region. On May 10, the IMF Bz component fluctuated and reached approximately -40 nT around 18:05 UTC, remaining negative from 19:05 UTC to 22:25 UTC, peaking at -40 nT. It then turned positive before reverting to negative at 23:40 UTC. During the northward IMF period, the Sym-H index showed a slight recovery. The southward IMF persisted until 04:35 UTC on May 11, during which the Sym-H index continued to decrease, reaching a minimum value of -412 nT at 02:00 UTC, with a slightly lower minimum of -415.5 nT observed simultaneously, which marked the end of the main phase and the storm's peak. Within 9 h, the Sym-H index rapidly decreased to -474 nT and -479.8 nT, respectively, highlighting the intense impact of the strong southward component of the IMF on Earth's magnetosphere.

3.2 Ionospheric response above Hong Kong

In low-latitude regions during years of high ionospheric activity, frequent ionospheric scintillation caused by plasma bubbles, triggered by multiple factors such as geomagnetic storms, is the dominant factor in how space weather events impact GNSS. Therefore, analyzing the ionospheric response

during this event is a top priority. In this study, we used GPS data with a 1-second interval, as mentioned in Section 2, to calculate three ionospheric indicators: (a) Vertical Total Electron Content (VTEC), (b) Rate of Total Electron Content Index (ROTI), and (c) S4 index.

(a) Vertical Total Electron Content (VTEC) represents background ionospheric effects (Liu et al., 2020). VTEC is calculated using the Dual-Frequency Code and Carrier Phase Linear Combination (DFCCL) method, a widely used approach for determining VTEC. This method assumes that the ionosphere is a single thin shell at an altitude of 450 km (Zhang, 2016; Zhou et al., 2023). The DFCCL method involves three key steps: (1) forming the geometry-free combination to remove frequency-independent terms, (2) eliminating satellite and receiver differential code biases (DCB), and (3) using the projection function to obtain Ionospheric Pierce Point (IPP) locations and corresponding VTEC values.

(b) The Rate of Total Electron Content Index (ROTI) characterizes the severity of GPS phase fluctuations and detects ionospheric irregularities marked by sharp TEC gradients. It is calculated as the standard deviation of the Rate of TEC (ROT) over a specific time interval using a running window mode (Pi et al., 1997).

$$ROTI = \sqrt{\langle ROT^2 \rangle - \langle ROT \rangle^2}, \tag{7}$$

$$ROT = \frac{STEC_k^i - STEC_{k-1}^i}{t_k - t_{k-1}},$$
(8)

where the superscript i denotes the PRN number of the GPS satellite, and the subscript k represents the k-th epoch. STEC stands for slant total electron content (TEC), t represents time, and $\langle \cdot \rangle$ denotes the average taken over a 5-minute time interval.

(c) The S4 index measures the intensity of ionospheric amplitude scintillation, which is typically dominant at low

Table 3. CME events during the first half of May 2024.

Event ID	CME Time	CME Speed	CME WD	Flare Time	Flare Class
1	2024-05-05 15:36 UTC DOY 126 23:36 LT	549	121	14:12	C7.5
2	2024-05-07 04:48 UTC DOY 128 12:48 LT	389	78	02:59	C9.5
3	2024-05-08 02:24 UTC DOY 129 10:24 LT	360	142	02:16	M3.4
4	2024-05-08 05:36 UTC DOY 129 13:36 LT	511	360	04:37	X1.0
5	2024-05-08 12:24 UTC DOY 129 20:24 LT	798	360	11:26	M8.7
6	2024-05-08 22:36 UTC DOY 130 06:36 LT	947	360	21:08	X1.0
7	2024-05-09 09:24 UTC DOY 130 17:24 LT	1226	360	08:45	X2.2
8	2024-05-09 12:24 UTC DOY 130 20:24 LT	833	123	11:52	M3.1
9	2024-05-09 19:18 UTC DOY 131 03:18 LT	1019	360	17:23	X1.1
10	2024-05-10 07:12 UTC DOY 131 15:12 LT	1006	360	06:27	X3.9
11	2024-05-11 01:36 UTC DOY 132 09:36 LT	1512	360	01:10	X5.8
12	2024-05-11 16:12 UTC DOY 132 00:12 LT	970	87	14:46	M8.8
13	2024-05-13 09:12 UTC DOY 134 17:12 LT	1812	360	08:48	M6.6
14	2024-05-14 01:48 UTC DOY 135 09:48 LT	341	68	01:23	M2.6
15	2024-05-14 02:24 UTC DOY 135 10:24 LT	929	87	02:03	X1.7
16	2024-05-14 13:00 UTC DOY 135 21:00 LT	792	55	12:40	X1.2
17	2024-05-14 17:00 UTC DOY 136 01:00 LT	1988	196	16:46	X8.7
18	2024-05-15 08:36 UTC DOY 136 16:36 LT	1724	360	08:13	X3.5
19	2024-05-15 10:48 UTC DOY 136 18:48 LT	1045	69	09:47	M3.6
20	2024-05-15 21:18 UTC DOY 137 05:18 LT	1359	360	20:30	C5.2

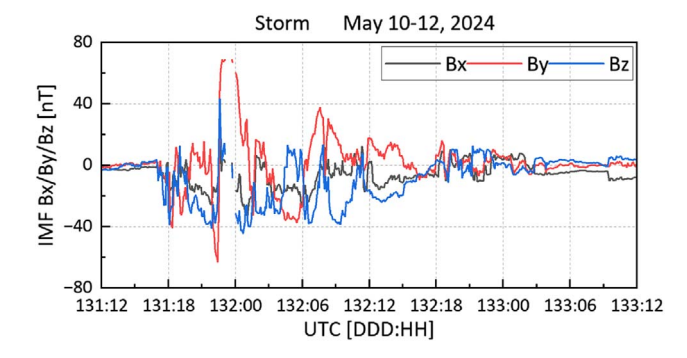




Figure 2. The IMF and Sym-H index during the geomagnetic storm.

latitudes. It is defined as the normalized variance of the signal intensity, represented by the following formula (Fremouw et al., 1978):

$$S4 = \sqrt{\frac{\langle I^2 \rangle - \langle I \rangle^2}{\langle I \rangle^2}},\tag{9}$$

where I denotes the signal intensity, and $\langle \cdot \rangle$ represents the average taken over a one-minute time interval.

We selected six evenly distributed stations in Hong Kong to analyze ionospheric conditions from 2024-05-01 to 2024-05-15.

Figure 3 shows the variations in ROTI and VTEC. During this period, maximum daily VTEC values reached around 90 TECU, indicating significant ionospheric ionization. Notable ROTI fluctuations occurred on DOY 122, 123, 124, 130, and 132, with peaks exceeding 5 TECU/min, confirming that space weather events in May enhanced ionospheric irregularities above Hong Kong. The minor fluctuations observed in ROTI, such as those around DOY 124 at 02:00 UTC (10:00 LT), may be attributed to the transient changes in TEC caused by solar flare eruptions.

Generally, a ROTI index of 0.25 or higher indicates ionospheric irregularities, suggesting the presence of EPBs in low-latitude regions (Liu et al., 2016). To provide a detailed overview of the daily ionospheric conditions, we compiled the times when ROTI exceeded 0.25 at the HKLM station during the study period (Fig. 4). Ionospheric irregularities persisted for longer durations on DOY 122–124, DOY 130, and DOY 132. Specifically, on DOY 130, these irregularities lasted approximately 400 min, whereas other days experienced minimal fluctuations. This may be attributed to the enhanced equatorial plasma fountain effect caused by the eastward prompt-penetration electric field (PPEF) prior to the geomagnetic storm induced by the CME's arrival. This leads to the enhanced $E \times B$ and the formation of EPB, triggering post-sunset ionospheric scintillation (Tahir et al., 2024).

Notably, the ionospheric response to the extreme geomagnetic storm that began on May 10, 2024 is highlighted in Figure 3. The orange line marks the storm's sudden commencement (SSC), and the green line indicates the moment of minimum Sym-H. It is clear that during the storm, there was no significant increase in ionospheric irregularities in the Hong Kong region. The calmness of the ionosphere above Hong Kong during the magnetic storm may be due to a reduced pre-reversal enhancement (PRE) electric field caused by the westward PPEF. Specifically, the post-sunset ionosphere drifted downward in altitude, creating unfavorable conditions for the Rayleigh–Taylor instability, thereby suppressing

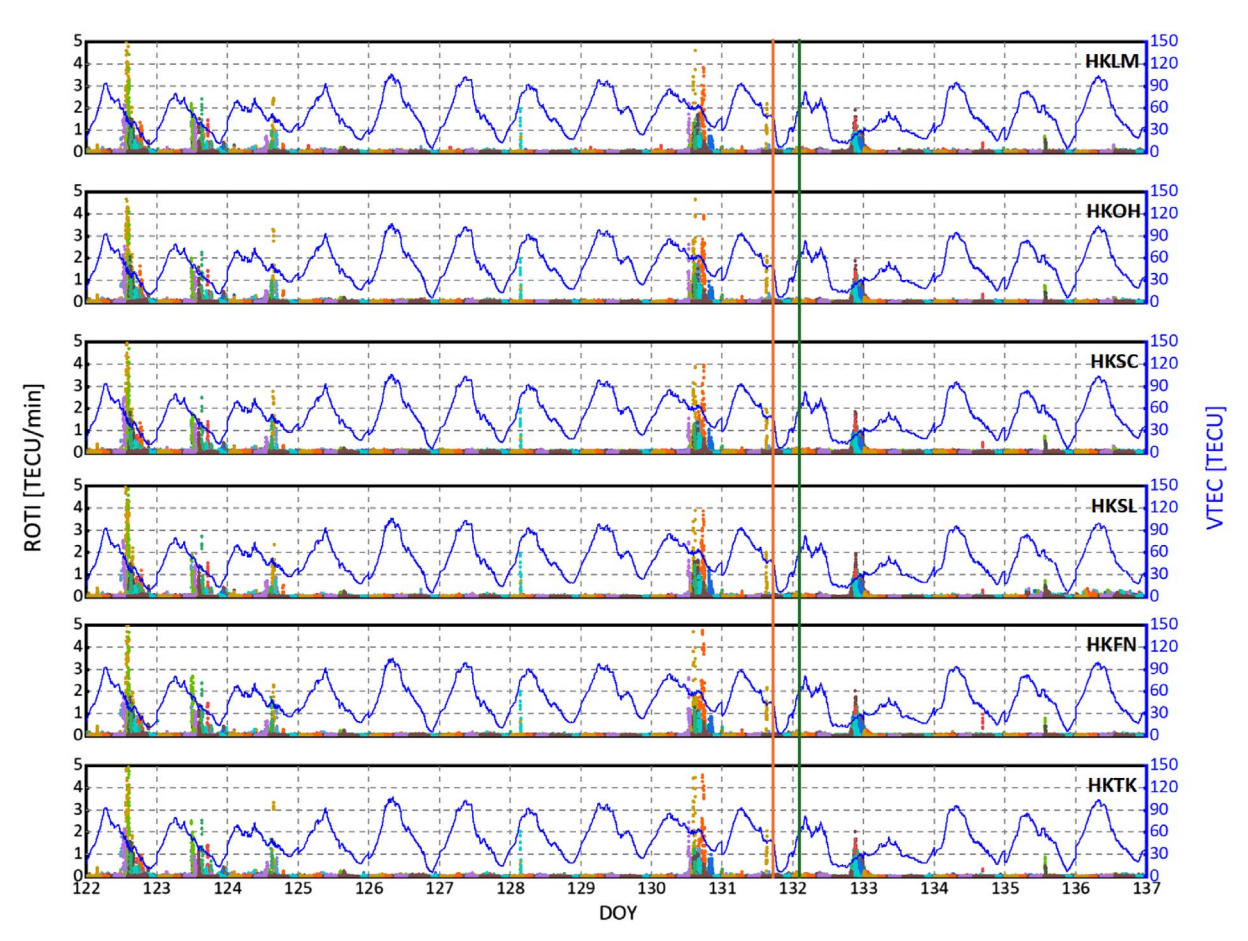


Figure 3. The VTEC and ROTI conditions at six stations in Hong Kong during the first half of May 2024 (DOY 122-136). The station name is displayed in the upper right corner of the figure. The blue curve represents VTEC, and the colored scatter points denote the ROTI index derived from different GPS satellites. The orange vertical line indicates the SSC onset time of the geomagnetic storm, while the green vertical line marks the time of minimum Dst during the storm.

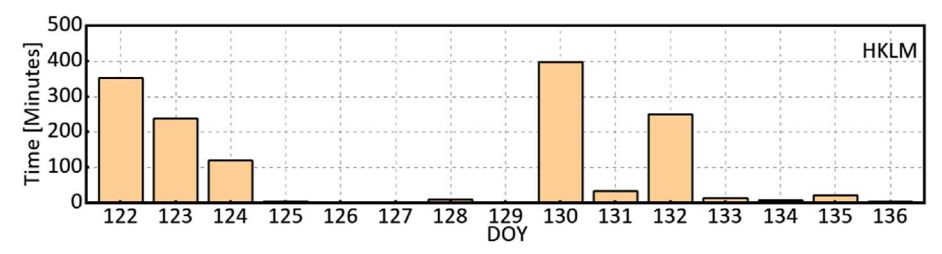


Figure 4. The daily statistics of times when ROTI exceeded 0.25 at the HKLM station during the experimental period. Each bar represents the time of a day (in minutes) when ROTI exceeded 0.25 within each 24-hour period. The threshold level of 0.25 is used to identify periods of enhanced ionospheric irregularities.

ionospheric irregularities. This situation is similar to the conditions observed during the 2015 St. Patrick's Day Geomagnetic Storm in the African equatorial regions, Taiwan, and Hong Kong (Nayak et al., 2017; Amaechi et al., 2018; Lu et al., 2020).

Since ionospheric EPBs generally lead to ionospheric scintillation, and amplitude scintillation is predominant at low latitudes, Figure 5 illustrates the S4 amplitude scintillation index at six selected GPS stations in Hong Kong from May 1 to

May 15. The station trends are consistent and strongly correlate with the ROTI index shown in Figure 3. This phenomenon indicates that the primary impact of space weather events in early May was likely ionospheric scintillation caused by nighttime EPBs above Hong Kong. During the extreme geomagnetic storm from May 10 to 12, 2024, prolonged ionospheric irregularities were observed only on DOY 132, primarily after 20:00 UTC (04:00 LT). Significant ionospheric TEC fluctuations occurred on the night of DOY 130.

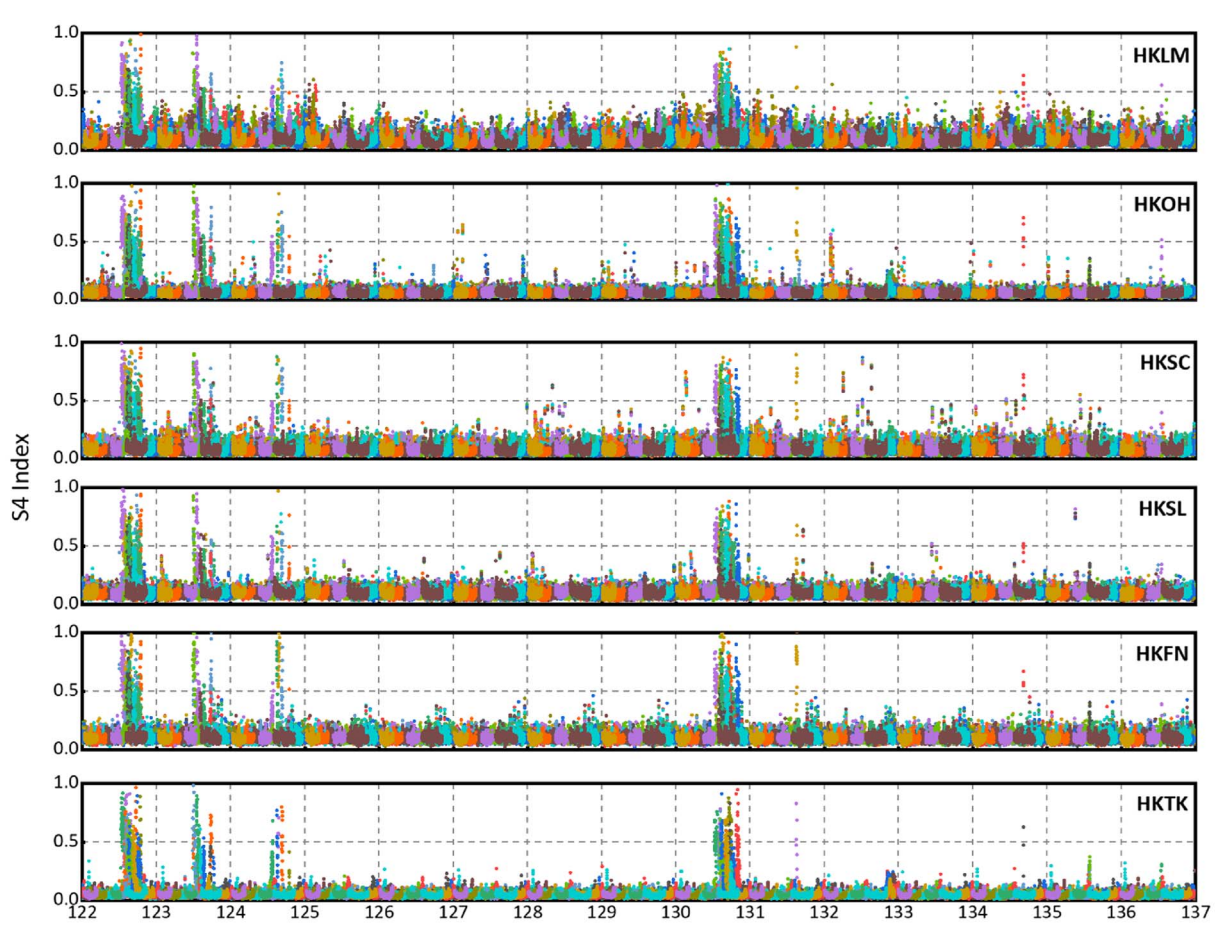


Figure 5. The S4 index at six stations in Hong Kong during the first half of May 2024 (DOY 122-136). The S4 index values are plotted as time series for each station, with higher values indicating stronger amplitude scintillation effects. Each color corresponds to a different GPS satellite. Data were sampled at 1 Hz and smoothed using a 5-minute moving average to reduce noise.

4 Real-time PPP methods

In this section, we first introduce the two PPP mathematical models used in the experiment in Section 4.1. Subsequently, Section 4.2 describes the ionospheric processing methods and strategies employed in these two models.

4.1 PPP models

In GNSS, pseudorange $P^i_{j,f}$ and carrier phase $\phi^i_{j,f}$ observations are fundamental for estimating receiver position, clock bias, and other parameters. The observation equations for these measurements can be formulated as follows (Xu & Xu, 2016; Sun et al., 2023):

$$P_{j,f}^{i} = \rho_{j}^{i} + c(\delta t_{j} - \delta t_{i}) + T_{j}^{i} + I_{j,f}^{i} + c(d_{j}^{f} - d_{i}^{f}) + \eta_{j,f}^{i},$$
(10)

$$\phi_{j,f}^{i} = \rho_{j}^{i} + c(\delta t_{j} - \delta t_{i}) + T_{j}^{i} - I_{j,f}^{i} + \lambda_{f} N_{j,f}^{i} + \delta_{j,f}^{i} + \epsilon_{j,f}^{i}.$$
(11)

Here, the superscripts i denote the satellite's PRN number, while the subscripts j and f represent the receiver ID and frequency

band, respectively. ρ^i_j is the geometric distance between satellite i and receiver j; c is the speed of light in a vacuum; δt_j and δt_i are the receiver and satellite clock biases, respectively; T^i_j is the zenith tropospheric delay; $I^i_{j,f}$ is the slant ionospheric delay at frequency f; λ_f is the wavelength of the signal at frequency f; $N^i_{j,f}$ is the integer ambiguity; d^f_j and d^f_i are the receiver and satellite hardware delays, respectively; and $\eta^i_{j,f}$ and $\epsilon^i_{j,f}$ account for measurement noise, multipath effects, and other unmodeled errors

To solve for the parameters in the observation equations, linearization is necessary. By incorporating the satellite orbit and clock corrections from the QZSS L6 correction, we obtain the dual-frequency UDUC-PPP model:

$$p_{j,f}^{i} = \mathbf{u}_{j}^{T} \cdot \mathbf{x} + c\delta t_{j} + m_{j} \cdot Z_{j} + I_{j}^{f} + \eta_{j}^{f}, \qquad (12)$$

$$\varphi_j^f = \mathbf{u}_j^T \cdot \mathbf{x} + c\delta t_j + m_j \cdot Z_j - I_j^f + \lambda_f N_j^f + \xi_j^f, \qquad (13)$$

where \mathbf{u}_j^T is the unit vector from the receiver to the satellite, \mathbf{x} denotes the position coordinates vector, δt_j is the receiver clock bias, Z_j indicates the tropospheric zenith delay, I_j^f is the ionospheric delay, N_j^f reflects the integer ambiguity, and η_j^f and ξ_j^f are the residual errors for pseudorange and carrier phase, respectively.

The Extended Kalman Filter (EKF) is employed for parameter estimation in this study (Takasu & Yasuda, 2009a). The state vector for the UDUC model is defined as follows:

$$\mathbf{X}_{\text{UCUD}} = \left[\mathbf{x}, \delta t_j, Z_j, I_j^f, N_j^f\right]^T. \tag{14}$$

For the IF-PPP model, the first-order ionospheric terms are eliminated through the following combination, which, after linearization, can be expressed as:

$$p_{j}^{\text{IF}} = \frac{f_{1}^{2}}{f_{1}^{2} - f_{2}^{2}} P_{j,1}^{i} - \frac{f_{2}^{2}}{f_{1}^{2} - f_{2}^{2}} P_{j,2}^{i} = \mathbf{u}_{j}^{T} \cdot \mathbf{x} + c \delta t_{j}^{\text{IF}} + m_{j} \cdot Z_{j} + \eta_{j}^{\text{IF}},$$
(15)

$$\phi_{j}^{\text{IF}} = \frac{f_{1}^{2}}{f_{1}^{2} - f_{2}^{2}} \phi_{j,1}^{i} - \frac{f_{2}^{2}}{f_{1}^{2} - f_{2}^{2}} \phi_{j,2}^{i}
= \mathbf{u}_{j}^{T} \cdot \mathbf{x} + c \delta t_{j}^{\text{IF}} + m_{j} \cdot Z_{j} + \lambda_{f} N_{j}^{\text{IF}} + \xi_{j}^{\text{IF}},$$
(16)

where $\delta t_j^{\rm IF}$ denotes the IF-combined receiver clock bias, and $N_j^{\rm IF}$ represents the IF-combined integer ambiguity. The state vector for the IF model is:

$$\mathbf{X}_{\mathrm{IF}} = \left[\mathbf{x}, \delta t_{j}^{\mathrm{IF}}, Z_{j}, N_{j}^{\mathrm{IF}}\right]^{T}.$$
(17)

Parameter estimation reveals that the IF-PPP model requires fewer parameters than the UCUD-PPP model because it does not need to estimate the ionospheric delay. However, since the observations in the IF-PPP model are combined, the number of observations is halved, resulting in increased noise.

4.2 Ionospheric delay and experimental strategies

Section 4.1 offers an in-depth analysis of the two PPP models utilized in this study. The UDUC model mitigates ionospheric delays through the estimation of these delays as additional parameters within the solution process. This method enables concurrent estimation of ionospheric delays but necessitates a larger dataset and is more sensitive to observation quality. In contrast, the IF model eliminates the primary ionospheric effect by computing an ionosphere-free combination. Higher-order ionospheric delays are significantly less pronounced compared to the first-order term.

Table 4 details the specific processing strategies employed. Kinematic PPP coordinates and receiver clock parameters are modeled as white noise. Tropospheric wet delay is represented using a random walk process. Carrier phase ambiguities are maintained as floating values, resulting in a non-constrained solution.

5 Impact and analysis of space weather events on real-time QZSS PPP

In this section, we analyze the impact of space weather events on dual-frequency IF-PPP in Section 5.1 and on UDUC-PPP in Section 5.2.

5.1 Impact and analysis on dual-frequency IF-PPP

We conducted a comprehensive evaluation of the IF-PPP accuracy in the Hong Kong region during space weather events.

Figure 6 illustrates the three-dimensional (3D) positioning errors for five selected stations in Hong Kong from DOY 122 to DOY 136 of 2024. Daily processing results in a convergence period at the start of each day, initially leading to larger 3D positioning errors. The variations in 3D errors show a strong positive correlation with the ROTI and S4 indices (Figs. 3 and 5). On DOY 122 and DOY 130, significant ionospheric effects caused positioning errors to exceed three meters, making precision positioning impossible. Additionally, the positioning results are influenced by factors such as receiver performance, accuracy of external products, and positioning algorithms. Consequently, performance varies at each station during days with ionospheric irregularities (DOY 123, 124, 130, and 132).

In order to numerically quantify the changes in positioning performance, we employed the commonly used Root Mean Square (RMS) of 3D positioning errors to represent the real-time PPP accuracy (Teunissen & Khodabandeh, 2015). Figure 7 shows the daily mean 3D RMS values of positioning errors for the 18 stations used in the experiment. The worst positioning accuracy occurred on DOY 122, with an RMS value approaching 0.3 m, coinciding with the day of highest ionospheric irregularities. The best accuracy was observed on DOY 128, with an RMS value of around 0.1 m. Positioning accuracy was approximately three times worse on days affected by space weather than on quiet days. Moreover, the accuracy of IF-PPP strongly correlates with the duration of ionospheric TEC fluctuations, as depicted in Figure 4, indicating that ionospheric TEC fluctuations significantly influence the accuracy of QZSS IF-PPP.

To investigate the reasons for degraded positioning accuracy, Figure 8 shows the positioning error plots for the HKLM and HKSL stations in the E, N, and U directions on DOY 122 and DOY 130. The accuracy experienced significant fluctuations between 12:00 and 16:00 UTC on DOY 122, coinciding with high ROTI values. These fluctuations occur during the local nighttime (20:00 to 04:00 LT), indicating that ionospheric scintillation caused by nighttime EPBs is responsible (Kintner et al., 2007). On DOY 130, similar increases in errors were observed at the same times but were less severe, likely due to less fluctuation in ionospheric electron density. However, for these two stations, the primary cause of degradation appears to be ionospheric disturbances from active space weather, particularly decreased observation quality due to scintillation. A detailed examination of this extreme event follows (Skone et al., 2001; Dubey et al., 2006).

We analyzed the reasons for the degradation in real-time IF-PPP accuracy. For post-processing PPP, (Zhang et al., 2014) identified three major reasons for significant accuracy degradation due to ionospheric scintillation: (a) Unexpected Loss of Lock: This occurs when satellites lose lock unexpectedly, reducing the number of available observations and increasing geometrical Dilution of Precision (GDOP). Typically, satellites with affected observations are excluded before positioning processing. (b) Failure of Cycle Slip Detection Algorithms: Large Rate of TEC (ROT) values can cause these algorithms to fail. Particularly, the ionospheric gradient during sunset and postsunset makes this issue more likely to occur (Liu et al., 2024). Additionally, ionospheric delays abruptly changing during ionospheric scintillation can lead to the failure of cycle slip detection algorithms, such as the geometry-free combination used in TurboEdit, which may retain significant ionospheric residuals (Blewitt, 1990). This reduces the reliability of cycle

Table 4. Experimental processing strategies.

Items	Strategies
Observations	IF: GPS L1/L2 ionosphere-free combination of code and carrier phase UDUC: GPS L1/L2 raw observations
Sampling rate	30 s
Elevation cutoff	10°
Observation weight	Elevation-dependent weight (Zhou et al., 2018)
Orbits	real-time QZSS L6 correction precise orbits
Satellite clocks	real-time QZSS L6 correction
Tidal loadings	IERS conventions (2010) and FES2004 model (Petit & Luzum, 2010)
Ionospheric delay	IF:Ionosphere-free combination mode UDUC: Estimate
Satellite antenna phase center correction	IGS20.atx
Receiver antenna phase center correction	IGS20.atx
Antenna phase wind-up correction	IGS model (Kouba, 2009)
Parameter estimation	Extended Kalman Filter (EKF) (Takasu & Yasuda, 2009)
Receiver coordinates	Estimate
Receiver clock	Estimate
Inter-system bias	Estimate
Ambiguities	Estimate, float
Tropospheric delay	Estimate ZTD and horizontal gradients (Niell, 1996)

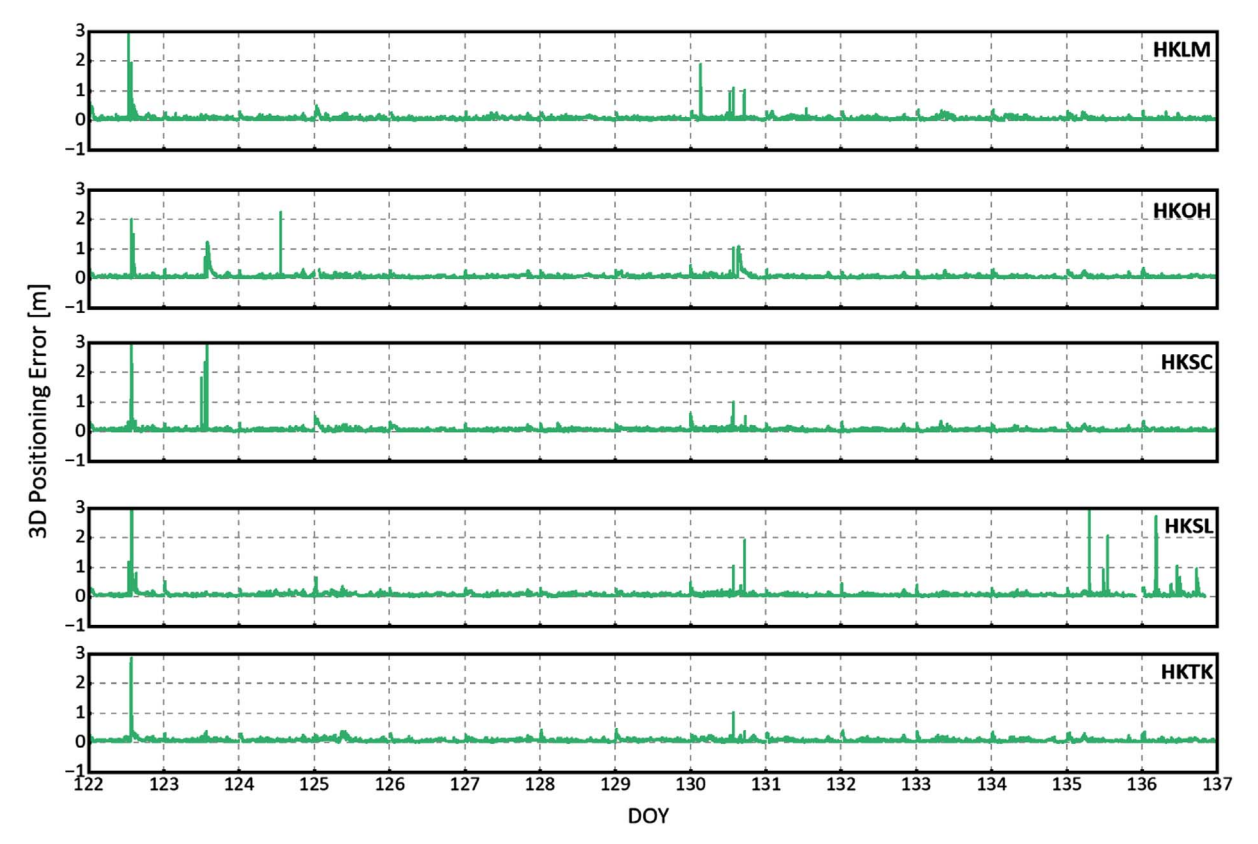


Figure 6. 3D positioning errors of IF-PPP at five stations during the first half of may 2024. The horizontal axis represents the DOY in 2024, and the vertical axis shows the 3D positioning errors, calculated as the differences between the IF-PPP results and reference coordinates in the E, N, and U components. Each line represents one station.

slip detection, causing unnecessary ambiguity reinitialization during positioning and resulting in degraded positioning performance. (c) Abnormal Blunders: These are not adequately mitigated in PPP estimation, leading to significant errors. Since there is no fundamental difference between real-time PPP and post-processed PPP in terms of positioning models and

methods, the degradation in real-time QZSS PPP positioning discussed in this paper can be analyzed using these potential causes.

Regarding (a) satellite loss of lock and (b) cycle slips, Figure 9 illustrates the number of satellites used for positioning at the HKLM station on DOY 122, as well as the cycle slips

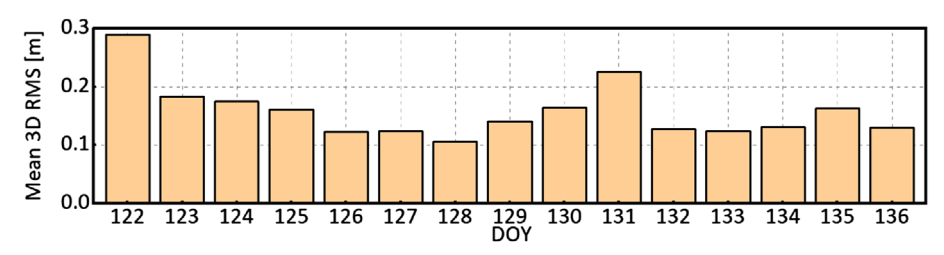


Figure 7. Daily mean RMS IF-PPP positioning accuracy across 18 stations during the experiment period. Each bar represents the average 3D RMS of the 18 stations for that day.

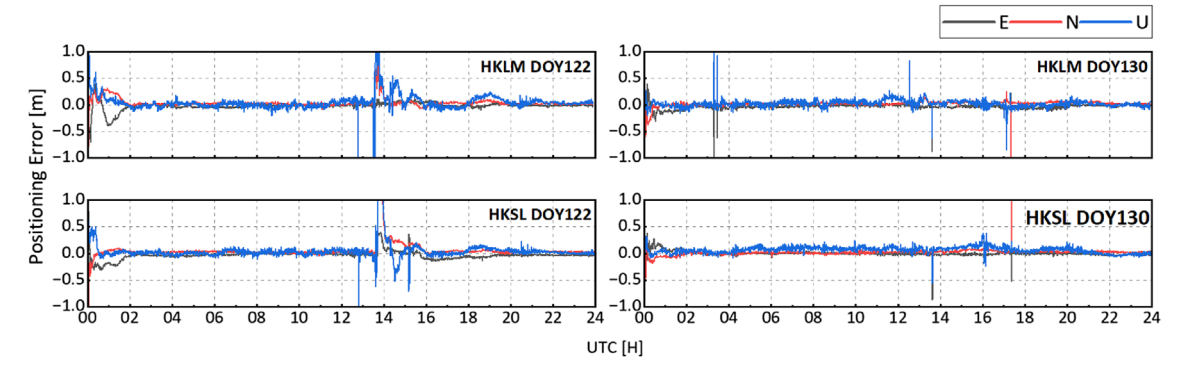


Figure 8. IF-PPP positioning errors in E, N, and U directions for HKLM and HKSL stations on DOY 122 and DOY 130. Each panel corresponds to one station-direction combination, and the fluctuations in positioning errors at 00:00 UTC each day are due to PPP convergence. The errors are computed as the difference between the IF-PPP results and reference positions.

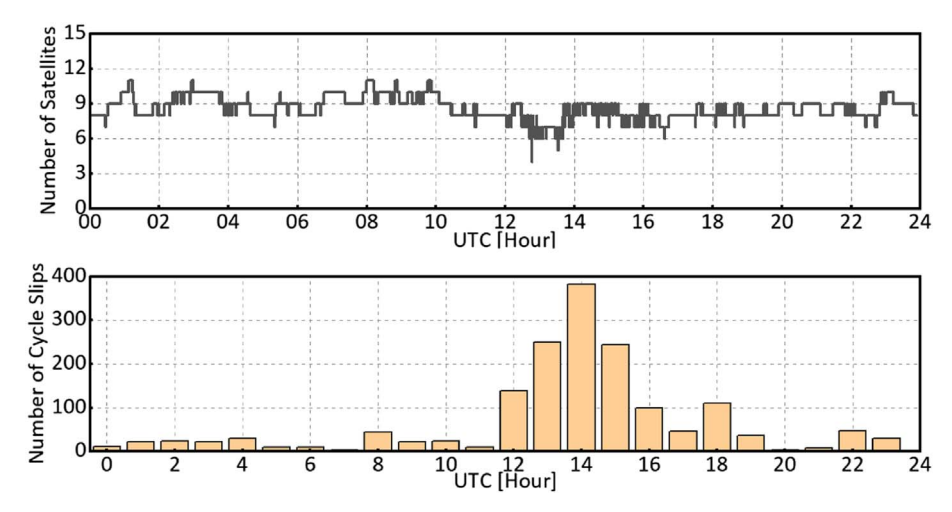


Figure 9. Number of satellites used for positioning and detected satellite cycle slips at HKLM station on DOY 122. The top plot shows the count of satellites utilized for positioning over time, while the bottom plot presents the number of cycle slips occurring per hour for all satellites.

detected using the TurboEdit algorithm. It can be observed that between 12:00 and 16:00 UTC (20:00 to 00:00 LT), the number of satellites decreases, and the number of detected cycle slips significantly increases, consistent with the variation in positioning errors (Fig. 8, top-left). This confirms that both factors (a) and (b) contribute to positioning degradation.

For further analysis, we examined the satellite usage at 12:47:30 UTC (20:47:30 LT), when the number of satellites available was minimal (Fig. 9, upper panel). Table 5 lists the GPS satellites used at different stages at this time. Among the seven satellites tracked in the RINEX file, G13, G15, and

Table 5. GPS satellites PRN used at different stages (example at 12:47:30 UTC).

Stage	GPS Satellite PRNs Used
Initial tracking Positioning calculation	G01, G07, G13, G15, G23, G28, G30 G01, G07, G28, G30

G23 were excluded during calculations due to poor signal quality caused by satellite loss of lock. Additionally, the lower part of Figure 9 shows that even the four satellites included in the

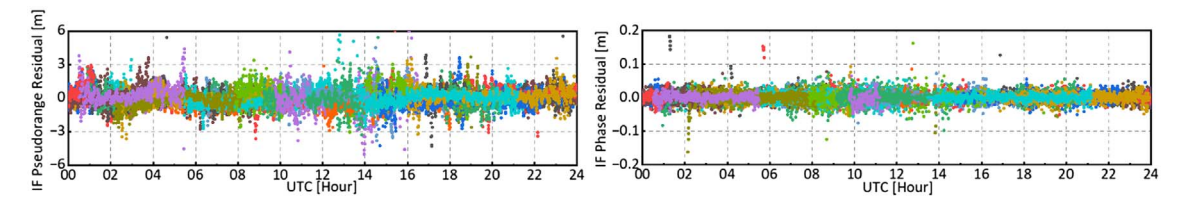


Figure 10. The pseudorange and phase residuals for the IF-PPP at HKLM station on DOY 122. The residuals are calculated as the differences between the observed and modeled values. Pseudorange residuals are shown on the left, while carrier phase residuals are shown on the right. Each satellite used in the solution is marked with a different color along the time axis. These residuals reflect the quality of the observation data and the performance of the IF-PPP model under ionospheric scintillation conditions.

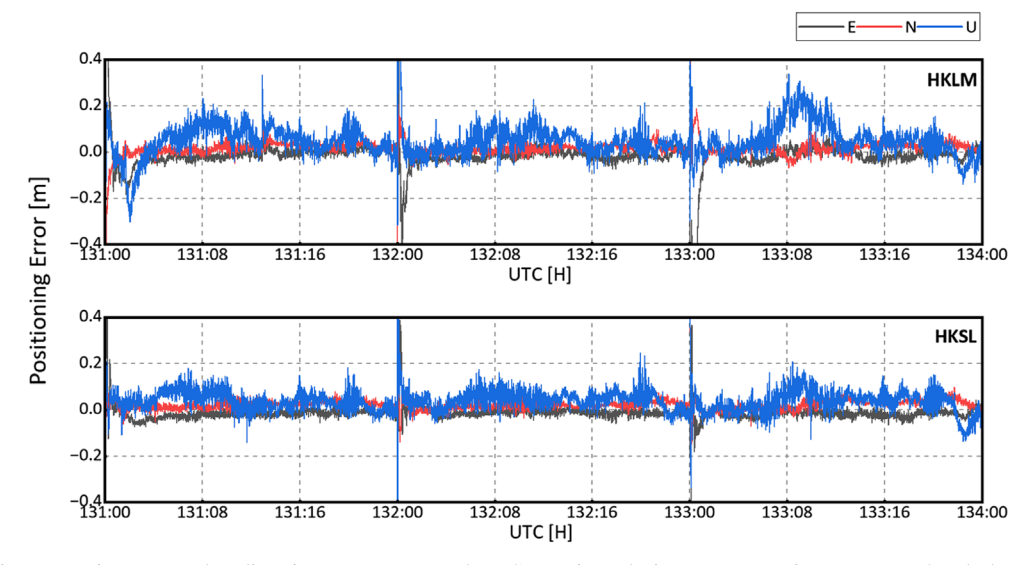


Figure 11. Position errors in E, N, and U directions at HKLM and HKSL stations during geomagnetic storms. Each subplot corresponds to one station, with different colors representing distinct directions. The fluctuations in positioning errors at 00:00 UTC each day are due to PPP convergence.

calculations detected cycle slips. This demonstrates that incorrect cycle slip detection leading to ambiguity re-initialization also contributed to the sudden drop in positioning accuracy (Zhang et al., 2014). Thus, the degradation mechanism can be explained by the combined effects of both factors, which should be considered during positioning processing.

Regarding (c) Abnormal Blunders, positioning residuals indicate the performance of PPP algorithms and the quality of raw observations. Figure 10 shows the pseudorange and phase residuals for the IF combination. Both types of residuals exhibit some fluctuations, with a few outliers. The pseudorange residuals are larger than the phase residuals, suggesting that the IF combination's algorithm is less affected by ionospheric scintillation.

Additionally, another potential reason could be the lower accuracy of orbits and clock products in real-time PPP. The main difference between real-time QZSS PPP and post-processed PPP is their implementation. Real-time QZSS PPP requires high-precision satellite orbits and clock corrections, which are obtained via satellite communication links. The lower precision of these real-time corrections can impact results. For instance, daily 3D-RMS values for real-time GPS and GLONASS orbits compared to post-processed products were 2.8 cm and 8.0 cm, respectively. The precision for QZSS L6

real-time corrections is 5.2 cm for orbits and 0.6 ns (~18 cm) for clocks (Bramanto & Gumilar, 2022; Kawate et al., 2023).

We also evaluated the accuracy of real-time QZSS PPP during the most significant extreme geomagnetic storm in the space weather events of 2024. Figure 11 shows that U-direction errors at the HKLM and HKSL stations were larger than in the E and N directions. The first significant error increase was at 08:00 UTC on DOY 131, before the storm's SSC event. During the storm's main phase, 3D-RMS errors were below 0.2 m. Another increase occurred on DOY 132 at 20:00 UTC, during the recovery phase, coinciding with ionospheric irregularities. After the storm subsided, the final fluctuation was around 10:00 UTC on DOY 133. Overall, positioning errors showed variability in the E, N, and U directions, before and after the storm. Additionally, at 00:00 UTC each day, peaks in positioning errors occur because our processing is conducted on a daily data basis, and the characteristics of the PPP algorithm lead to a convergence period (typically within one hour) at the start of processing. For PPP, achieving stable and accurate results depends heavily on precise satellite orbit and clock correction data, as well as modeling of tropospheric and ionospheric delays, which generally requires a longer convergence time (Kouba & Héroux, 2001).

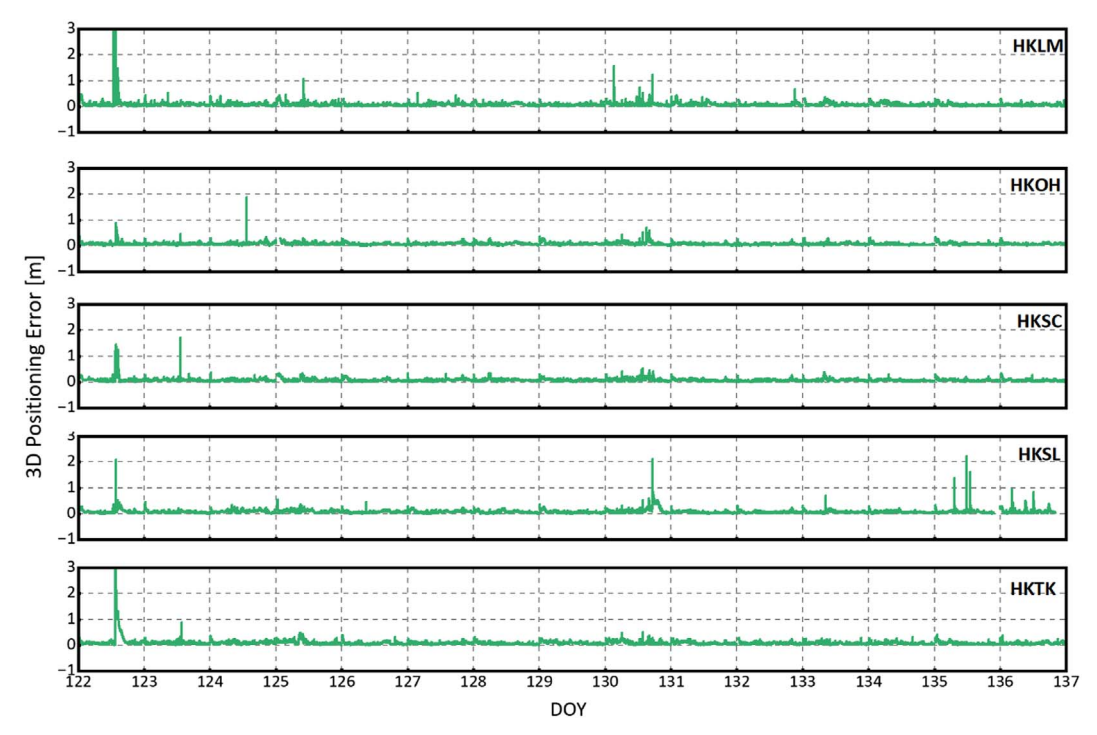


Figure 12. 3D positioning errors of UDUC-PPP at five stations during the first half of May 2024. The 3D errors are computed as the square root of the sum of squared errors in the E, N, and U components. Each line represents one station.

5.2 Impact and analysis on dual-frequency UDUC-PPP

We conducted a comprehensive evaluation of the UDUC-PPP accuracy in the Hong Kong region during space weather events. Figure 12 shows the 3D positioning errors of QZSS UDUC-PPP for five stations in Hong Kong during early May 2024. The errors increased during high ROTI and S4 values, such as on DOY 122 and DOY 130, indicating a positive correlation with TEC fluctuations.

In evaluating the numerical statistics of positioning performance, we computed the daily mean RMS values for the 3D positioning accuracy across all 18 stations. As depicted in Figure 13, there is a substantial reduction in accuracy on days characterized by high ROTI and S4 values, with DOY 122 emerging as the most adversely affected. When compared to IF-PPP, the accuracy of UDUC-PPP deteriorates by approximately 16% over the span of 15 days, resulting in an average accuracy of roughly 0.19 m. This decline in performance may be ascribed to the more parameters estimated by UDUC-PPP, which consequently extends the convergence time. The heightened positioning errors during this extended convergence period could have influenced these statistics.

We further scrutinized the positioning errors in the E, N, and U directions for the HKLM and HKSC stations on DOY 122 and DOY 130. As illustrated in Figure 14, during the nighttime of DOY 122 and 130, there was a substantial increase in the N and U direction errors. Notably, the U-direction errors at the HKLM and HKSL stations are more pronounced than those in the E and N directions. In addition, compared to the positioning errors of IF-PPP at the same time and stations (as seen in Fig. 8), UDUC-PPP exhibits smaller severe errors. For instance, at HKLM and HKSL on DOY 132 between 14:00 and

16:00 UTC (22:00 and 14:00 LT), the positioning errors of IF-PPP have already exceeded 3 m, whereas the maximum positioning error for UDUC-PPP remains within 1 meter. This discrepancy could be due to the differing impact mechanisms between IF-PPP and UDUC-PPP. In the case of IF-PPP, the process of combination results in halved observations, and the reduction due to scintillation leads to errors extending beyond the meter level. Conversely, UDUC-PPP retains more observations under scintillation conditions, resulting in less pronounced error increases compared to IF-PPP.

With IF-PPP, Figure 9 shows that the periods of increased frequency of changes in the number of satellites used for positioning and increased cycle slips coincide with the times of ionospheric irregularity variations. Figure 15 indicates that UDUC-PPP phase residuals have few outliers, while pseudorange residuals change significantly between 12:00 and 16:00 UTC. The L2 pseudorange shows more variation than L1, indicating a higher susceptibility to disturbances. The UDUC-PPP model struggles to mitigate these variations during ionospheric scintillation, contributing to its slightly inferior positioning accuracy compared to IF-PPP.

Compared to IF-PPP, UDUC-PPP differs mainly in two aspects: (1) UDUC-PPP does not require signal combinations, thereby avoiding noise amplification and preserving all information contained in the original observations; (2) ionospheric delays cannot be eliminated in UDUC-PPP and must be estimated as unknown parameters. Given that ionospheric delays vary with different frequencies, the main feature of IF-PPP is the formation of an ionosphere-free combination to eliminate ionospheric delays. In contrast, the observables in UDUC-PPP do not involve an ionosphere-free combination. Consequently, the PPP results based on the UDUC model include ionospheric

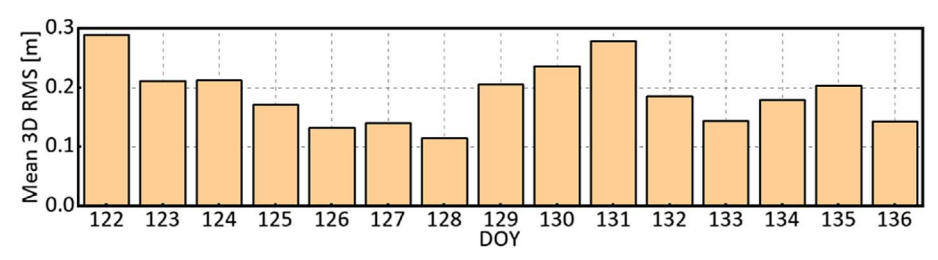


Figure 13. Daily mean RMS positioning accuracy across all 18 GPS stations during the experiment period. Each bar represents the average 3D RMS of the 18 stations for that day.

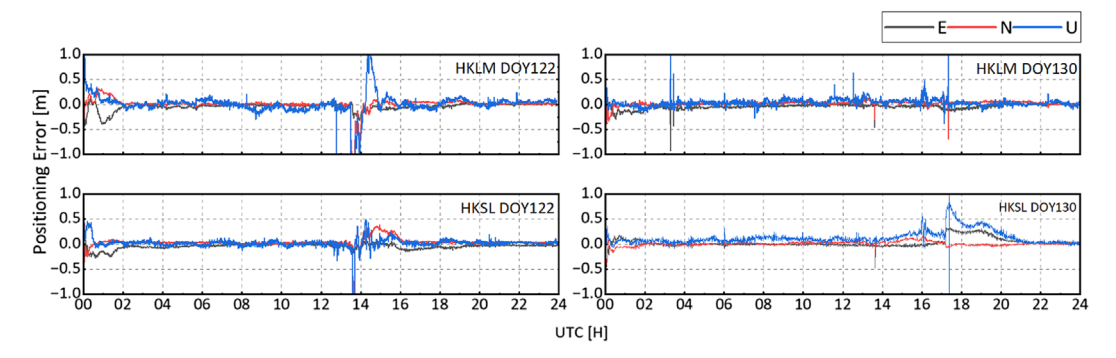


Figure 14. Positioning errors in the E, N, and U directions for HKLM and HKSL stations on DOY 122 and DOY 130. Each subplot corresponds to a station-day-direction combination, with the x-axis representing time of day (in hours) and the y-axis showing the positioning error in meters. The reference coordinates used for error computation were derived from high-precision post-processing.

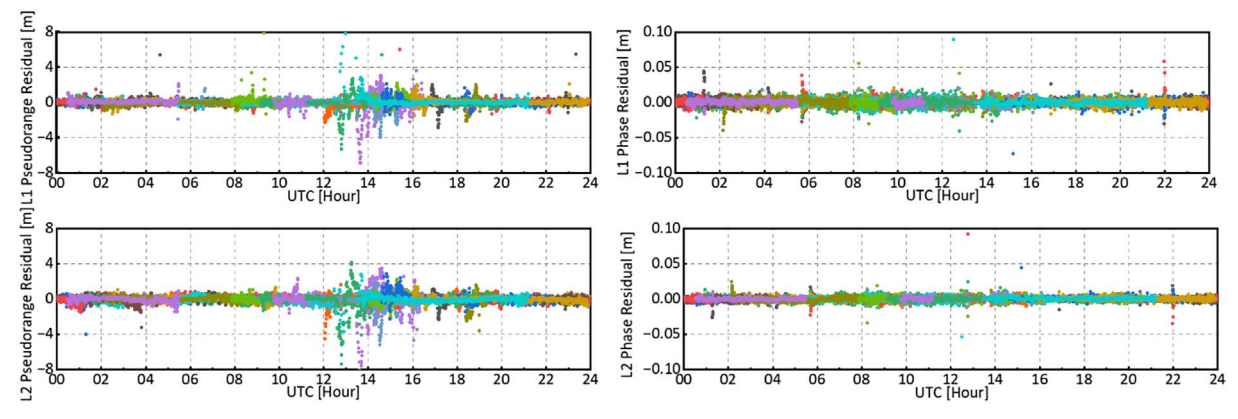


Figure 15. The pseudorange and phase residuals for the L1 and L2 at HKLM station on DOY122. The residuals represent the differences between the measured and modeled observations after removal of all known effects. Each satellite tracked during the day is labeled separately along the time axis. These residuals provide insight into the quality of the observational data and the performance of the observation model under typical ionospheric conditions.

delays. Numerous studies have demonstrated that under normal conditions without additional external constraints, both models yield nearly identical PPP positioning performance (Guo et al., 2016). However, our analysis reveals distinct behaviors during ionospheric scintillation events. Statistical results during the experimental period indicate that IF-PPP generally exhibits slightly better positioning performance, evidenced by smaller RMS values (Figs. 7 and 13). This may be due to UDUC-PPP requiring the estimation of more parameters than IF-PPP, leading to longer convergence times and extended reinitialization periods following ionospheric disturbances. During

ionospheric scintillation events, UDUC-PPP shows less severe errors and longer initialization times (Fig 8 and 14), likely because UDUC-PPP retains more observations without combination while also needing more time for parameter estimation during initialization.

6 Conclusions

For the severe space weather events in May 2024, we analyzed ionospheric responses above Hong Kong and evaluated

the positioning performance of widely used real-time PPP. The findings are summarized as follows:

- 1. Space weather events in early May 2024 significantly affected the real-time QZSS PPP accuracy of both IF-PPP and UDUC-PPP approaches, which demonstrated a strong correlation with S4. This accuracy deterioration is mainly attributed to satellite loss of lock and failure of cycle slip detection algorithms, leading to poor GDOP and ambiguity reinitialization, as well as a decline in observation quality. Additionally, the lower precision of real-time satellite orbits and clock corrections further impaired positioning results. Notably, L1 pseudorange measurements were more resistant to scintillation effects than L2.
- 2. We highlighted the different ways in which ionospheric delay and scintillation affect IF and UDUC during May 2024 space weather events. Regarding scintillation, the degradation in real-time QZSS PPP accuracy is primarily due to the deteriorated observation quality caused by ionospheric scintillation. However, the impact mechanisms differ between IF-PPP and UDUC-PPP. In the case of IF-PPP, the combination process results in halving the number of used observations, and the reduction due to scintillation leads to errors exceeding the meter level. In contrast, UDUC-PPP retains more observations under scintillation conditions, resulting in less severe error increases compared to IF-PPP. As for delays, UDUC does not use the IF combination, which means that the positioning results retain ionospheric delays and experience longer convergence times during reinitialization.
- 3. Space weather events could have two main effects on the ionosphere: changes in the ionospheric background TEC and irregular ionospheric variations. Our analysis indicates that while the changes in the background TEC result in changes in the ionospheric delay, they do not have a significant impact on positioning. In contrast, irregular ionospheric variations, such as ionospheric scintillation, dominate the degradation in positioning accuracy. During the space weather events, solar flares and CMEs impact the ionosphere and positioning differently. Solar flares rapidly increase electron density in the dayside ionosphere through electromagnetic radiation, affecting positioning in the short term. In contrast, CME-driven geomagnetic storms occur a few days after the CME, closely associated with ionospheric storms. During this period, the EIA becomes more pronounced, with steeper ionospheric gradients on the north and south sides of the EIA, increasing the likelihood of EPB. Analysis of the ionospheric response indicates that irregularities above the Hong Kong region were likely due to amplitude scintillations caused by nighttime EPBs. Notably, the extreme geomagnetic storm from May 10 to May 12 did not significantly impact the ionosphere, possibly due to the westward PPFE suppressing the occurrence of Rayleigh-Taylor instabilities.

To improve real-time positioning during ionospheric scintillation, we plan to integrate QZSS real-time PPP characteristics with predictions and forecasts of ionospheric changes. This approach aims to mitigate positioning performance degradation during such periods.

Acknowledgments

We acknowledge the Hong Kong Satellite Positioning Reference Station Network for providing the GPS data, the Center for Orbit Determination in Europe (CODE) for the satellite Differential Code Bias (DCB) products, the International GNSS Service (IGS) for the antenna exchange (ATX) files, and the Quasi-Zenith Satellite System (QZSS) for the L6 correction data. The editor thanks two anonymous reviewers for their assistance in evaluating this paper.

Funding

This work was supported by the National Key Research and Development Program of China (2022YFF0503904), the Guangxi Science and Technology Base and Talent Special Project (Gui Ke AD25069103), and the Shenzhen Science and Technology Program (JCYJ20241202123731040, KJZD20240903104015020).

Data availability statement

The GPS data were obtained from the Hong Kong Satellite Positioning Reference Station Network, available at https://rinex.geodetic.gov.hk/. The satellite Differential Code Bias (DCB) products were sourced from the Center for Orbit Determination in Europe (CODE) and can be accessed at https://ftp.aiub.unibe.ch/CODE/. The antenna exchange format (ATX) files are publicly available from the International GNSS Service (IGS) at https://files.igs.org/pub/station/general. The QZSS L6 Correction Data were acquired from the QZSS-Archives, accessible at https://sys.qzss.go.jp/dod/en/archives.html. The Interplanetary Magnetic Field (IMF) and SYM-H index data were obtained from the OMNIWeb database, which is located at https://omniweb.gsfc.nasa.gov.

References

- Aa, E, Zou S, Liu S. 2020. Statistical analysis of equatorial plasma irregularities retrieved from Swarm 2013–2019 observations. *J Geophys Res Space Phys* **125** (4): e2019JA027,022. https://doi.org/10.1029/2019JA027022.
- Afraimovich, E, Demyanov V, Ishin A, Smolkov G. 2008. Powerful solar radio bursts as a global and free tool for testing satellite broadband radio systems, including GPS-GLONASS-GALILEO. *J Atmos Sol-Terr Phys* **70** (15): 1985–1994. https://doi.org/10.1016/j.jastp.2008.09.008.
- Alkan, RM, Erol S, İlçi V, Ozulu İM. 2020. Comparative analysis of real-time kinematic and PPP techniques in dynamic environment. *Measurement* 163: 107,995. https://doi.org/10.1016/j.measurement. 2020.107995.
- Amaechi, P, Oyeyemi E, Akala A. 2018. The response of African equatorial/low-latitude ionosphere to 2015 St. Patrick's Day geomagnetic storm. *Space Weather* **16 (6)**: 601–618. https://doi.org/10.1029/2017SW001751.
- Aquino, M, Monico J, Dodson A, Marques H, De Franceschi G, Alfonsi L, Romano V, Andreotti M. 2009. Improving the GNSS positioning stochastic model in the presence of ionospheric scintillation. *J Geod* 83: 953–966. https://doi.org/10.1007/s00190-009-0313-6.
- Balasis, G, Papadimitriou C, Boutsi AZ. 2019. Ionospheric response to solar and interplanetary disturbances: a Swarm perspective. *Philos Trans R Soc A Math Phys Eng Sci* **377 (2148)**: 20180,098. https://doi.org/10.1098/rsta.2018.0098.
- Blewitt, G. 1990. An automatic editing algorithm for GPS data. *Geophys Res Lett* **17** (3): 199–202. https://doi.org/10.1029/GL017i003p00199.

- Bojilova, R, Mukhtarov P, Pancheva D. 2024. Global ionospheric response during extreme geomagnetic storm in May 2024. *Rem Sens* **16** (21): 4046. https://doi.org/10.3390/rs16214046.
- Bramanto, B, Gumilar I . 2022. Evaluation of QZSS orbit and clock products for real-time positioning applications. *J Appl Geod* **16** (3): 165–179. https://doi.org/10.1515/jag-2021-0064.
- Brueckner, G, Howard R, Koomen M, Korendyke C, Michels D, et al. 1995. The Large Angle Spectroscopic Coronagraph (LASCO). In: *The SOHO Mission*, Fleck B, Domingo V, Poland A (Eds.), Springer Netherlands, Dordrecht, 357–402. ISBN 978-94-009-0191-9. https://doi.org/10.1007/978-94-009-0191-9_10.
- Chen, D, Guo W, Xie Z, Xia P, Luo X, Ye S, Jiang W, Liu H. 2023. Ionospheric irregularities responses to strong geomagnetic storms in Hong Kong region over the past two solar cycles (2001–2020). *IEEE Trans Geosci Rem Sens* **61**: 1–9. https://doi.org/10.1109/TGRS.2023.3244233.
- De Bakker, PF, Tiberius CC. 2017. Single-frequency GNSS positioning for assisted, cooperative and autonomous driving. In : Proceedings of the 30th International Technical Meeting of the Satellite Division of The Institute of Navigation (ION GNSS+2017), pp. 4038–4045. https://doi.org/10.33012/2017.15151.
- Demyanov, V, Yasyukevich YV. 2021. Space weather: Risk factors for global navigation satellite systems. *Sol-Terr Phys* **7** (2): 28–47. https://doi.org/10.12737/stp-72202104.
- Dubey, S, Wahi R, Gwal A. 2006. Ionospheric effects on GPS positioning. *Adv Space Res* 38 (11): 2478–2484. https://doi.org/10.1016/j.asr.2005.07.030.
- Elsobeiey, M, Al-Harbi S. 2016. Performance of real-time precise point positioning using IGS real-time service. *GPS Solu* **20**: 565–571. https://doi.org/10.1007/s10291-015-0467-z.
- Fernandez-Hernandez, I, Chamorro-Moreno A, Cancela-Diaz S, Calle-Calle JD, Zoccarato P, et al. 2022. Galileo high accuracy service: initial definition and performance. *GPS Solu* **26** (3): 65. https://doi.org/10.1007/s10291-022-01247-x.
- Follestad, AF, Clausen LBN, Moen JI, Jacobsen KS. 2021. Latitudinal, diurnal, and seasonal variations in the accuracy of an RTK positioning system and its relationship with ionospheric irregularities. *Space Weather* **19 (6)**: e2020SW002625. https://doi.org/10.1029/2020SW002625.
- Förster, M, Jakowski N. 2000. Geomagnetic storm effects on the topside ionosphere and plasmasphere: A compact tutorial and new results. Surv Geophys 21: 47–87. https://doi.org/10.1023/A:1006775125220.
- Fremouw, E, Leadabrand R, Livingston R, Cousins M, Rino C, Fair B, Long R. 1978. Early results from the DNA Wideband satellite experiment Complex-signal scintillation. *Radio Sci* **13** (1): 167–187. https://doi.org/10.1029/RS013i001p00167.
- González, GDL. 2022. Storm-time variability of ionospheric irregularities over South America. *J Atmos Sol-Terr Phys* **241**: 105,980. https://doi.org/10.1016/j.jastp.2022.105980.
- Gosling, JT. 1993. The solar flare myth. *J Geophys Res Space Phys* **98** (A11): 18937–18949. https://doi.org/10.1029/93JA01896.
- Guo, F, Zhang X, Wang J, Ren X. 2016a. Modeling and assessment of triple-frequency BDS precise point positioning. *J Geod* 90: 1223–1235. https://doi.org/10.1007/s00190-016-0920-y.
- Guo, F, Zhang X, Wang J, Ren X. 2016. Modeling and assessment of triple-frequency BDS precise point positioning, *J Geod* **90** (11): 1223–1235. https://doi.org/10.1007/s00190-016-0920-y.
- Hayakawa, H, Ebihara Y, Mishev A, Koldobskiy SA, Kusano K, et al. 2024. The solar and geomagnetic storms in May 2024: a flash data report. https://api.semanticscholar.org/CorpusID:271088675.
- Iyemori, T, Takeda M, Nose M, Odagi Y, Toh H. 2010. Mid-latitude geomagnetic indices "ASY" and "SYM" for 2009 (Provisional). In: Data Analysis Center for Geomagnetism and Space Magnetism,

- Graduate School of Science, Kyoto University, Japan. https://wdc.kugi.kyoto-u.ac.jp/wdc/pdf/indexplot/20%20Mid-latitude%20Geomagnetic%20Indices%20ASY%20and%20SYM%20(Provisional) (2009).pdf .
- Jacobsen, KS, Andalsvik YL. 2016. Overview of the 2015 St. Patrick's day storm and its consequences for RTK and PPP positioning in Norway. J. Space Weather Space Clim 6: A9. https://doi.org/10.1051/swsc/2016004.
- Jacobsen, Dähnn. 2014. Statistics of ionospheric disturbances and their correlation with GNSS positioning errors at high latitudes. J. Space Weather Space Clim 4: A27. https://doi.org/10.1051/swsc/2014024.
- Kawate, K, Igarashi Y, Yamada H, Akiyama K, Okeya M, et al. 2023. MADOCA: Japanese precise orbit and clock determination tool for GNSS. Adv Space Res 71 (10): 3927–3950. https://doi.org/ 10.1016/j.asr.2023.01.060.
- Kintner, PM, Ledvina BM, De Paula E. 2007. GPS and ionospheric scintillations. *Space Weather* **5** (9): S09003. https://doi.org/10.1029/2006SW000260.
- Kouba, J. 2009. *A guide to using International GNSS Service (IGS)* products. https://files.igs.org/pub/resource/pubs/UsingIGSProductsVer21_cor.pdf.
- Kouba, J, Héroux P. 2001. Precise point positioning using IGS orbit and clock products. GPS Solu 5: 12–28. https://doi.org/10.1007/ PL00012883.
- Lazzús, J, Salfate I. 2024. Report on the effects of the May 2024 Mother's day geomagnetic storm observed from Chile. J Atmos Sol-Terr Phys 261: 106–304. https://doi.org/10.1016/j.jastp.2024.106304.
- Leick, A, L Rapoport, Tatarnikov D. 2015. Real-time kinematics relative positioning. In: *GPS Satellite Surveying, chap. 7*, John Wiley & Sons, Ltd, pp. 401–474. ISBN 978-1-119-01861-2. https://doi.org/10.1002/9781119018612.ch7.
- Lejeune, S, Warnant R. 2008. A novel method for the quantitative assessment of the ionosphere effect on high accuracy GNSS applications, which require ambiguity resolution. *J Atmos Sol-Terr Phys* **70** (6): 889–900. https://doi.org/10.1016/j.jastp.2007.01.009.
- Liu, L, Zou S, Yao Y, Aa E. 2020. Multi-scale ionosphere responses to the May 2017 magnetic storm over the Asian sector. *GPS Solu* **24**: 1–15. https://doi.org/10.1007/s10291-019-0940-1.
- Liu, T, Jiang Y, Ma Y, Yu Z, Xu G. 2022. Maximum eigenvalue detection for local ionospheric anomaly theory, cases, statistics, and potential application. *Measurement* **203**: 111990. https://doi.org/10.1016/j.measurement.2022.111990.
- Liu, T, Mi X, Yang Y, Weng D, Chen W. 2024. Model the ionospheric gradients between satellites in network RTK. In: Proceedings of the 37th International Technical Meeting of the Satellite Division of The Institute of Navigation (ION GNSS+ 2024), pp. 3092–3100. https://doi.org/10.33012/2024.19847.
- Liu, T, Yu Z, Ding Z, Nie W, Xu G. 2021. Observation of ionospheric gravity waves introduced by thunderstorms in low latitudes China by GNSS. *Rem Sens* 13 (20): 4131. https://doi.org/ 10.3390/rs13204131.
- Liu, T, Zhang B, Yuan Y, Li M. 2018. Real-Time Precise Point Positioning (RTPPP) with raw observations and its application in real-time regional ionospheric VTEC modeling. *J Geod* 92: 1267– 1283. https://doi.org/10.1007/s00190-018-1118-2.
- Liu, X, Yuan Y, Tan B, Li M. 2016. Observational analysis of variation characteristics of GPS-based TEC fluctuation over China. *ISPRS Int J Geo-Inform* 5 (12): 237–https://doi.org/10.3390/ ijgi5120237.
- Lu, Y, Wang Z, Ji S, Chen W. 2020. Assessing the positioning performance under the effects of strong ionospheric anomalies with multi-GNSS in Hong Kong. *Radio Sci* 55 (8): e2019RS007,004. https://doi.org/10.1029/2019RS007004.

- Luo, X, Lou Y, Xiao Q, Gu S, Chen B, Liu Z. 2018. Investigation of ionospheric scintillation effects on BDS precise point positioning at low-latitude regions. GPS Solu 22 (3): 63. https://doi.org/ 10.1007/s10291-018-0728-8.
- Machol, JL, Eparvier FG, Viereck RA, Woodraska DL, Snow M, et al. 2020. GOES-R series solar X-ray and ultraviolet irradiance. In: *The GOES-R Series*, Elsevier, pp. 233–242. https://doi.org/10.1016/B978-0-12-814327-8.00019-6.
- Matamba, TM, Danskin DW, Nndanganeni RR, Tshisaphungo M. 2023. Space weather impacts on the ionosphere over the Southern African mid-latitude region. *Earth Planet Space* **75** (1): 142. https://doi.org/10.1186/s40623-023-01894-5.
- Montenbruck, O, Hauschild A, Steigenberger P. 2014. Differential code bias estimation using multi-GNSS observations and global ionosphere maps. *NAVIGATION: J Inst Navig* **61 (3)**: 191–201. https://doi.org/10.1002/navi.64.
- Muellerschoen, RJ, Bar-Sever YE, Bertiger WI, Stowers DA. 2001. NASA's global DGPS for high-precision users. *GPS World* **12** (1): 14. https://link.gale.com/apps/doc/A69551678/AONE?u=anon57b 74f2asid=googleScholar xid=b6c2c828.
- Muhammad, B, Alberti V, Marassi A, Cianca E, Messerotti M. 2015. Performance assessment of GPS receivers during the September 24, 2011 solar radio burst event. *J Space Weather Space Clim* 5: A32. https://doi.org/10.1051/swsc/2015034.
- Namie, H, Kubo N. 2021. Performance evaluation of centimeter-level augmentation positioning L6-CLAS/MADOCA at the beginning of official operation of QZSS. *IEEJ J Ind Appl* **10** (1): 27–35. https://doi.org/10.1541/ieejjia.20001080.
- Nayak, C, Tsai L-C, Su S-Y, Galkin I, Caton R, Groves K. 2017. Suppression of ionospheric scintillation during St. Patrick's Day geomagnetic super storm as observed over the anomaly crest region station Pingtung, Taiwan: A case study. *Adv Space Res* 60 (2): 396–405. https://doi.org/10.1016/j.asr.2016.11.036.
- Nie, W, Rovira-Garcia A, Wang Y, Zheng D, Yan L, Xu T. 2022. On the global kinematic positioning variations during the September 2017 solar flare events. *J Geophys Res Space Phys* **127** (8): e2021JA030,245. https://doi.org/10.1029/2021JA030245.
- Nie, W, Wang F, Qiao Z, Xu T, Wang Y, Ye M, Hu L, Liu T. 2024. Ionospheric irregularities coinciding with the 2023 Typhoon Saola: a multi-instrument study. *J Geophys Res Space Phys* 129 (12): e2024JA033,043. https://doi.org/10.1029/2024JA033043.
- Niell, AE. 1996. Global mapping functions for the atmosphere delay at radio wavelengths. *J Geophys Res Solid Earth* **101** (**B2**): 3227– 3246. https://doi.org/10.1029/95JB03048.
- Pan, L, Cai C, Santerre R, Zhang X. 2017. Performance evaluation of single-frequency point positioning with GPS, GLONASS, BeiDou and Galileo. Surv Rev 49 (354): 197–205. https://doi.org/10.1080/ 00396265.2016.1151628.
- Paziewski, J, Sieradzki R. 2020. Enhanced wide-area multi-GNSS RTK and rapid static positioning in the presence of ionospheric disturbances. *Earth Planet Space* **72**: 1–16. https://doi.org/10.1186/s40623-020-01238-7.
- Petit, G, Luzum B. 2010. *IERS conventions* (2010). http://www.iers.
- Pi, X, Mannucci A, Lindqwister U, Ho C. 1997. Monitoring of global ionospheric irregularities using the worldwide GPS network. *Geophys Res Lett* 24 (18): 2283–2286. https://doi.org/10.1029/ 97GI 02273
- Rothacher, M, Schmid R. 2010. ANTEX: The antenna exchange format, version 1.4. Format specifications. IGS Central Bureau, Pasadena 2006. https://files.igs.org/pub/data/format/antex14.txt.
- Sato, H, Jakowski N, Berdermann J, Jiricka K, Heßelbarth A, Banys' D, Wilken V. 2019. Solar radio burst events on 6 September 2017

- and its impact on GNSS signal frequencies. *Space Weather* **17 (6)**: 816–826. https://doi.org/10.1029/2019SW002198.
- Schuh, MA, Angryk RA, Martens PC. 2016. A large-scale dataset of solar event reports from automated feature recognition modules. J Space Weather Space Clim 6: A22. https://doi.org/10.1051/swsc/ 2016015.
- Schwenn, R. 2006. Space weather: The solar perspective. *Liv Rev Sol Phys* **3** (1): 1–72. https://doi.org/10.12942/lrsp-2006-2.
- Sergeeva, MA. 2022. Space weather general concepts. In: *Space Weather Impact on GNSS Performance*, V, Demyanov, Yasyukevich Y, Sergeeva MA, Vesnin A (Eds.), Springer International Publishing, Cham, 89–150. ISBN 978-3-031-15874-2. https://10.1007/978-3-031-15874-2_3.
- Skone, S, Knudsen K, De Jong M. 2001. Limitations in GPS receiver tracking performance under ionospheric scintillation conditions. *Phys Chem Earth A Solid Earth Geod* **26** (**6–8**): 613–621. https://doi.org/10.1016/S1464-1895(01)00110-7.
- Smith, J, Heelis RA. 2017. Equatorial plasma bubbles: Variations of occurrence and spatial scale in local time, longitude, season, and solar activity. *J Geophys Res Space Phys* **122** (5): 5743–5755. https://doi.org/10.1002/2017JA024128.
- Sun, M, Liu L, Yan W, Liu J, Liu T, Xu G. 2023. Performance analysis of BDS B1C/B2a PPP using different models and MGEX products. Surv Rev 55 (389): 192–203. https://doi.org/10.1080/ 00396265.2022.2081013.
- Tahir, A, Wu F, Shah M, Amory-Mazaudier C, Jamjareegulgarn P, Verhulst TGW, Ameen MA. 2024. Multi-instrument observation of the ionospheric irregularities and disturbances during the 23–24 March 2023 Geomagnetic Storm. Rem Sens 16 (9): 1594. https://doi.org/10.3390/rs16091594.
- Takasu, T, Yasuda A. 2009a. Development of the low-cost RTK-GPS receiver with an open source program package RTKLIB. In: *International Symposium on GPS/GNSS*, Vol. 1. International Convention Center Jeju Korea Seogwipo-si, Republic of Korea, pp. 1–6. https://gpspp.sakura.ne.jp/paper2005/isgps_2009_rtklib_revA.pdf.
- Takasu, T, Yasuda A. 2009. Development of the low-cost RTK-GPS receiver with an open source program package RTKLIB. https://api.semanticscholar.org/CorpusID:37732623.
- Teunissen, P, Khodabandeh A. 2015. Review and principles of PPP-RTK methods. *J Geod* **89** (3): 217–240. https://doi.org/10.1007/s00190-014-0771-3.
- Tsurutani, BT, Verkhoglyadova OP, Mannucci AJ, Lakhina GS, Li G, Zank GP. 2009. A brief review of "solar flare effects" on the ionosphere. *Radio Sci* **44** (1): RS0A17. https://doi.org/10.1029/2008RS004029.
- Warnant, R, Lejeune S, Bavier M. 2007. Space weather influence on satellite-based navigation and precise positioning. In: *Space Weather: Research Towards Applications in Europe*, J, Lilensten (Ed.), Springer Netherlands, Dordrecht, pp. 129–146. ISBN 978-1-4020-5446-4. https://10.1007/1-4020-5446-7_14.
- Xu, G, Xu Y. 2016. GPS observation equations and equivalence properties. In: GPS: Theory, Algorithms and Applications, G, Xu, Y Xu (Eds.), Berlin, Heidelberg, Springer. ISBN 978-3-662-50367-6. https://10.1007/978-3-662-50367-6_6.
- Yang, Y, Ding Q, Gao W, Li J, Xu Y, Sun B. 2022. Principle and performance of BDSBAS and PPP-B2b of BDS-3. *Satellite Navigation* **3** (1): 5. https://doi.org/10.1186/s43020-022-00066-2.
- Yasyukevich, Y, Astafyeva E, Padokhin A, Ivanova V, Syrovatskii S, Podlesnyi A. 2018. The 6 September 2017 X-class solar flares and their impacts on the ionosphere, GNSS, and HF Radio Wave Propagation. *Space Weather* **16 (8)**: 1013–1027. https://doi.org/10.1029/2018SW001932.

- Zakharenkova, I, Cherniak I. 2021. Effects of storm-induced equatorial plasma bubbles on gps-based kinematic positioning at equatorial and middle latitudes during the September 7–8, 2017, geomagnetic storm. *GPS Solu* **25** (**4**): 132. https://doi.org/10.1007/s10291-021-01166-3.
- Zhang, B. 2016. Three methods to retrieve slant total electron content measurements from ground-based GPS receivers and performance assessment. *Radio Sci* 51 (7): 972–988. https://doi.org/10.1002/ 2015RS005916.
- Zhang, X, Guo F, Zhou P. 2014. Improved precise point positioning in the presence of ionospheric scintillation. *GPS Solu* **18**: 51–60. https://doi.org/10.1007/s10291-012-0309-1.
- Zhou, C, Yang L, Li B, Balz T. 2023. M_GIM: a MATLAB-based software for multi-system global and regional ionospheric

- modeling. GPS Solu 27 (1): 42. https://doi.org/10.1007/s10291-022-01370-9.
- Zhou, F, Dong D, Li W, Jiang X, Wickert J, Schuh H. 2018. GAMP: An open-source software of multi-GNSS precise point positioning using undifferenced and uncombined observations. *GPS Solu* 22: 1–10. https://doi.org/10.1007/s10291-018-0699-9.
- Zumberge, J, Heflin M, Jefferson D, Watkins M, Webb FH. 1997. Precise point positioning for the efficient and robust analysis of GPS data from large networks. *J Geophys Res Solid Earth* **102** (B3): 5005–5017. https://doi.org/10.1029/96JB03860.
- Zuo, Z, Yang B, Li Z, Zhang T. 2022. A GNSS/IMU/vision ultratightly integrated navigation system for low altitude aircraft. *IEEE Sens J* 22 (12): 11857–11864. https://doi.org/10.1109/JSEN.2022. 3168605.

Cite this article as: Sun M, Liu T, Liu J, Zhang K, Huang J, et al. 2025. Real-time precise point positioning performance in Hong Kong during May 2024 space weather events. *J. Space Weather Space Clim.* **15**, 36. https://doi.org/10.1051/swsc/2025033.

Annexes: Detailed Explanation of Table 4

To better understand the data and its implications presented in Table 4, we provide herein a detailed explanation and background information for unclear entries.

(a) Explanation of "Estimate": The term "Estimate" in the table refers to parameters that need to be estimated during the computation process rather than removed using models beforehand. For instance, Tidal loadings are removed using the IERS conventions (2010) and FES2004 model, whereas Receiver clock and Inter-system bias are estimated along with Receiver coordinates through the positioning algorithm. The specific parameters that need to be estimated are detailed in equations (14) and (17) in the main text. The primary distinction between IF-PPP and UDUC-PPP in parameter estimation lies in the handling of ionospheric delay. IF-PPP removes the first-order ionospheric delay through the ionosphere-free combination, thus eliminating the need for estimation.

(b) Introduction to Real-Time QZSS L6 Corrections: The real-time QZSS L6 corrections mentioned in the table under orbits and Satellite

clocks refer to external products used in PPP. Since PPP requires precise external products for high-accuracy positioning, post-processed PPP typically uses the sp3 format precise ephemeris and clock corrections provided by IGS analysis centers, which have a lag of about 14 days. In contrast, real-time OZSS L6 corrections are broadcast from QZSS satellites in RTCM-SSR standard format at a transmission rate of 2000 bits/s. Each message consists of a 49-bit header, a 1695-bit data section, and a 256-bit Reed-Solomon code. Currently, L6E provides orbit corrections, clock corrections, code phase biases, and user range accuracy for GPS, GLONASS, and QZSS, with update intervals of 30s, 2s, 10800s, and 30s, respectively. These corrections are based on positions and clock errors calculated from broadcast ephemeris and require selecting a set of matching parameters in the broadcast ephemeris according to the SSR-provided ephemeris age to compute satellite clock errors and positions. The specific algorithm for correcting satellite orbits and clock errors using L6E corrections is described in detail in Section 2.2.